

Local Analysis of MISR Surface BRF and Albedo Over GSFC and Mongu AERONET Sites

Alexei Lyapustin, Yujie Wang, John Martonchik, Jeffrey L. Privette, *Member, IEEE*, Brent Holben, Ilya Slutsker, Alexander Sinyuk, and Alexander Smirnov

Abstract—We have developed an atmospheric correction algorithm to retrieve the surface bidirectional reflectance factor (BRF) and albedo from Multiangle Imaging SpectroRadiometer (MISR) measurements for small areas around Aerosol Robotic Network (AERONET) sunphotometer sites, using AERONET aerosol and column water vapor information. Our goal is to develop an indirect validation method for MISR surface reflectance products over heterogeneous land. Our algorithm makes independent retrievals with both the Li Sparse–Ross Thick kernel BRF model and the modified Rahman–Pinty–Verstraete BRF model used in the Moderate Resolution Imaging Spectroradiometer and MISR land algorithms, respectively. In this study, we report the first results of processing MISR Collection 4 data for 2003–2004 for two sites, Mongu, Zambia, and Greenbelt, MD. We found that MISR generally provides accurate retrievals of BRF and albedo in both clear and hazy atmospheric conditions, correctly reproducing the parameter time series and spatial distribution. We found that the MISR BRF, on average, is less anisotropic in the visible bands. The difference is greatest in the blue band, but decreases with increasing wavelength such that it is negligible in the near-IR band. This discrepancy originates in part in the MISR aerosol retrieval algorithm over heterogeneous land, which tends to select an aerosol model that favors spectrally invariant shapes of surface BRF. The other part of the discrepancy comes from the surface hemispherical-directional reflectance factor retrieval algorithm where the iteration loop that removes the diffuse atmospheric transmittance is currently turned off. Our initial results suggest that the MISR surface albedo is on average lower than our retrievals by about 0.005 in the green and red bands. In the near-IR, it agreed with our retrievals with the modified Rahman–Pinty–Verstraete model for the Mongu site, but was systematically lower over the Greenbelt site by about 0.016. When significant aerosol absorption is present (Mongu), the albedo discrepancy is additionally biased by the difference between the MISR and AERONET retrievals of aerosol absorption.

Index Terms—Aerosol Robotic Network (AERONET), albedo, atmospheric correction, bidirectional reflectance, Multiangle Imaging SpectroRadiometer (MISR), validation

I. INTRODUCTION

VALIDATION is a critical component of the Earth Observing System (EOS) [1] aimed at establishing the accuracy of satellite-derived products on the regional and

Manuscript received October 25, 2004; revised June 14, 2005. This work was supported by NASA EOS Science (Dr. D. Wickland) and NASA NPP (Dr. R. Murphy) grants.

A. Lyapustin, Y. Wang, and A. Smirnov are with the GEST University of Maryland Baltimore County, Catonsville, MD 21228 USA, and also with the NASA Goddard Space Flight Center, Greenbelt, MD 20771 USA.

J. Martonchik is with the Jet Propulsion Laboratory, California Institute of Technology, Pasadena, CA 91109 USA.

J. L. Privette and B. Holben are with the NASA Goddard Space Flight Center, Greenbelt, MD 20771 USA.

I. Slutsker and A. Sinyuk are with the SSAI/NASA Goddard Space Flight Center, Greenbelt, MD 20771 USA.

Digital Object Identifier 10.1109/TGRS.2005.856678

global scales, under different atmospheric and surface conditions. Due to spatial heterogeneity of the land surface, validation of surface reflectance is a difficult and challenging task. Measurements of albedo from the ground or towers [2] can be used as validation data at a moderate resolution (≈ 1 km) only for relatively homogeneous surfaces. Field measurements are sparse globally, and each represents only local conditions. We are not aware of any detailed ground-based measurements of surface bidirectional reflectance factor (BRF) and albedo to characterize heterogeneous land. A comprehensively planned validation experiment would have to cover the area of at least several satellite footprints with a statistically representative grid of points and a sampling interval comparable to the scale of surface variability (e.g., several tens of meters). Such an approach, which would amount to several thousand measurements concurrent with the satellite overpass, does not seem feasible. Moreover, the ground-based measurements of surface directional reflectance made under natural solar illumination conditions need to be atmospherically corrected to derive the BRF [3]. This implies more complex measurements with concurrent characterization of aerosol and water vapor.

In this paper, we present an alternative approach of indirect validation of Multiangle Imaging SpectroRadiometer (MISR) surface reflectance products over Aerosol Robotic Network (AERONET) sunphotometer [4] sites. The idea is to collect the best ancillary information on atmospheric aerosol and water vapor, and perform an independent atmospheric correction (AC) of MISR measurements based on accurate radiative transfer theory that is not constrained by the time requirements of operational processing. Of course, our approach is not a full validation based on independent well-calibrated measurements of surface reflectance. However, it has merits that ground-based measurements do not provide, such as the capacity to allow spatial analysis over relatively large nonhomogeneous area of study. In general, with this approach we will be able to verify that 1) MISR aerosol retrievals do not change the spectral and spatial pattern of derived surface reflectance, and 2) the assumptions and operational simplifications of the MISR algorithm do not produce biases when compared to rigorous radiative transfer codes. The same spatial and spectral resolution is a strong advantage because it allows direct comparison of results. With this perspective, applying this approach to different instruments, such as Moderate Resolution Imaging Spectroradiometer (MODIS) and MISR, may help cross calibration of on-orbit sensors.

Below, we present an analysis of MISR BRF and albedo over the Mongu (Zambia) and Greenbelt, MD (hereafter referred to

as GSFC) test sites for 2003 and 2004. The size of each study area is 32×32 pixels at MISR's composite resolution of 1.1 km. Among the different EOS Land Validation Core Sites [2] for which MISR subsetted data are freely provided by Langley Data Center, Mongu and GSFC have the greatest number of clear days in 2003–2004 with reprocessed MISR Collection 4 data. Atmospheric conditions in Mongu change dramatically in the end of the dry season when the biomass burning occurs. The surface also exhibits considerable spatial and temporal variability, from urban areas that have little seasonal change to an extensive flood plain with strong seasonal vegetative dynamics. The GSFC site has a considerable spatial variability, and typically, clear atmospheric conditions with low-absorbing aerosols.

The theory and specific implementation of the processing algorithm are described in Section II of this paper. Examples of BRF/albedo retrievals and comparisons with MISR results are given in Section III. This section also provides an analysis of the spatial distribution and time series of albedo. Section IV discusses the effect of BRF model on the retrieval results. The paper is concluded by a summary.

II. DESCRIPTION OF ALGORITHM

Our AC algorithm for MISR data constrained by AERONET ancillary information is based on a new Green's function solution for the radiance over nonhomogeneous and anisotropic surfaces [5], [6]. In this study, we use a one-dimensional (1-D) Green's function solution [5], or an independent pixel approximation, which should be quite accurate because the surface contrast over the areas of study is not very high, and the spatial resolution (1.1 km) of the MISR data is relatively low. The full three-dimensional (3-D) AC algorithm that takes adjacency effect into account is still under testing.

A. Expression for the TOA Radiance

In the 1-D Green's function solution, the top of the atmosphere (TOA) radiance at a given wavelength is expressed as a sum of path radiance (D) and surface-reflected radiance, directly and diffusely transmitted through the atmosphere

$$L(s_0, s) = D(s_0, s) + e^{-\tau/|\mu|} L_s(s_0, s) + L_s^d(s_0, s). \quad (1)$$

Here, τ is the optical thickness, and incidence (s_0) and view (s) directions are described by pairs of zenith and azimuthal angles (θ , φ). The cosine of the zenith angle $\mu = \cos \theta$ is negative for upward directions and positive for downward directions. The surface-reflected radiance is expressed as

$$L_s(s_0, s) \cong S_\lambda \mu_0 e^{-\tau/\mu_0} \{ \rho(s_0, s) + \alpha c_0 \rho_1(\mu) \rho_2(\mu_0) \} + \frac{\alpha}{\pi} \int_{\Omega^+} D_s(s_0, s') \rho(s', s) \mu' ds' \quad (2)$$

where πS_λ is extraterrestrial solar spectral irradiance, D_s is the surface-incident path radiance, ρ is the surface BRF, and

$$\rho_1(\mu) = \frac{1}{2\pi} \int_{\Omega^+} \rho(s', s) ds', \quad \rho_2(\mu_0) = \frac{1}{2\pi} \int_{\Omega^-} \rho(s_0, s) ds \quad (3)$$

α is a multiple reflection factor, $\alpha = (1 - q(\mu_0)c_0)^{-1}$ depending on the surface albedo (q) and spherical albedo of the atmosphere

(c_0). The diffusely transmitted surface-reflected radiance at the TOA is calculated from L_s with the help of 1-D diffuse Green's function of the atmosphere

$$L_s^d(s_0, s) = \int_{\Omega^-} G^d(s_1, s) L_s(s_0, s_1) ds_1. \quad (4)$$

In the literature, function G^d is often called bidirectional diffuse transmittance of the atmosphere in the upward directions. The surface albedo is defined conventionally as a ratio of reflected and incident surface fluxes

$$q(\mu_0) = \frac{F^{Up}(\mu_0)}{F^{Down}(\mu_0)} \quad (5a)$$

$$F^{Down}(\mu_0) = \pi S_\lambda \mu_0 e^{-\tau/\mu_0} + \int_{\Omega^+} D_s(s_0, s') \mu' ds' \quad (5b)$$

$$F^{Up}(\mu_0) = \pi S_\lambda \mu_0 e^{-\tau/\mu_0} q_2(\mu_0) + \int_{\Omega^+} \mu' q_2(\mu') D_s(s_0, s') ds' \quad (5c)$$

$$q_2(\mu_0) = \frac{1}{\pi} \int_{\Omega^-} \rho(s_0, s) \mu ds.$$

For further detail and other notations, readers may consult [5] and [6]. Below, we will also use another form of (1) with the direct surface-reflected term singled out

$$L(s_0, s) = D(s_0, s) + S_\lambda \mu_0 e^{-\tau(1/\mu_0 + 1/|\mu|)} \rho(s_0, s) + R(s_0, s) \quad (6)$$

where R stands for the other terms of (1) related to the diffuse surface-reflected radiance.

B. Algorithm of AC

The implementation of the AC algorithm, and to some extent its results, depend on the chosen parametric model of BRF. Presently, two models are widely used in the operational processing of the EOS data. The Li Sparse–Ross Thick reciprocal (LSRT) model [7] is adopted in the MODIS land algorithm [8], and the modified Rahman–Pinty–Verstraete (MRPV) [9] model is used in the MISR land processing [10]. Both MODIS and MISR instruments provide global datasets of BRF and albedo. These datasets differ in a number of ways. For example, the multiangular MISR sensor captures the instantaneous angular signature of land targets, whereas the MODIS BRF is retrieved from a 16-day collection of samples, a period over which surface changes can occur. The BRF model is one of the difference factors in the two datasets whose role was not yet investigated on a large scale with satellite data.

Keeping this in mind, along with our plans to analyze the MODIS products in the future, we developed two independent algorithms of AC of MISR data, based on LSRT and MRPV models. The LSRT is a linear semi-empirical model represented as a sum of Lambertian, geometric-optical, and volume scattering components

$$\rho(s', s) = k_L + k_{go} f_{go}(s', s) + k_v f_v(s', s). \quad (7)$$

It uses predefined “kernels” f_{go} , f_v to describe different angular shapes, the concept first suggested by Roujean *et al.* [11]. The kernels are independent of the land conditions. The BRF of a pixel is characterized by a combination of three kernel weights,

$\vec{K} = \{k_L, k_{go}, k_v\}^T$. The substitution of (7) into (1) yields a quasilinear equation with respect to the unknown vector parameter \vec{K}

$$\vec{L} = \hat{C}\vec{K} \quad (8)$$

where $\vec{L} = \{L_1, \dots, L_9\}$ is an array of MISR measurements at nine view angles. \hat{C} is a 9×3 matrix, with elements represented by the integrals of the incident path radiance, Green's function, and kernel functions, at different view angles. Matrix \hat{C} weakly depends on \vec{K} due to multiple reflections from the surface, usually via a multiple reflection factor α , and can be represented as a sum, $\hat{C} = \hat{A} + \hat{B}(\vec{K})$. Elements of matrix $\hat{B}(\vec{K})$ are small compared to those of matrix \hat{A} , $b_{ij}(\vec{K})/a_{ij} \approx qc_0$. The use of LSRT model leads to a very efficient iterative retrieval algorithm with an explicit least-squares formulation for the kernel weights, which in matrix form is written as

$$\text{RMSE}_L = \left\| \vec{L} - \hat{C}^{(n-1)}\vec{K}^{(n)} \right\| = \min. \quad (9)$$

Here, n is the iteration number, and matrix \hat{C} is calculated using \vec{K} values from the previous iteration. Because the nonlinear terms are small, the convergence is achieved in 2–3 iterations even in conditions of very high atmospheric turbidity over bright surfaces. The algorithm is fast because the matrix elements are calculated only once, and then they are scaled with the new values of the kernel weights. After the kernel weights are found, and the diffuse component of the surface-reflected radiance calculated in the process, the BRF is calculated at MISR view angles from the direct surface-reflected term of (6). This function is not smoothed by the least-squares fit, and retains the specific angular features of the measurements.

MRPV is an empirical model expressed as a product of three different functions. This model is nonlinear with respect to its parameters, but it can be linearized by a logarithmic transformation. The AC algorithm with this model consists essentially of iterations between the direct and diffuse components of radiance reflected from surface. In the n th iteration, the BRF is calculated from the direct reflected radiance

$$\rho_i^{(n)} = \frac{(L_i - D_i - R_i^{(n-1)})}{S_{\lambda}\mu_0 e^{-\tau(1/\mu_0 + 1/|\mu_i|)}}. \quad (10)$$

The three parameters of MRPV model $\{r_0, k, b\}$ are then computed with the logarithms $\ln(\rho_i^{(n)})$ as described in the MISR Algorithm Theoretical Basis Document [10]. The new MRPV parameters are used to calculate the diffuse surface signal for the next iteration, $R_i^{(n)}$, etc. In each iteration, we calculate the root mean square error, RMSE_L , between the MISR measurements and the calculations with the MRPV BRF model. The initial estimate of the MRPV parameters is obtained from the BRF retrieved with the LSRT model.

Though conceptually simple, this minimization problem is rather challenging. At high values of optical thickness, the solution becomes unstable. One can see from (10) how small errors in the calculation of path radiance and diffuse surface-reflected radiance are amplified at large τ , especially at high solar or view zenith angles. These errors may be due to inaccurate knowledge of aerosol parameters, or inability of the BRF model to

reproduce the correct angular pattern of surface reflectance. Due to the nature of (10), the solution oscillates around the best-fit values as the iterations progress. To reduce oscillations and improve convergence, we use a relaxation method

$$\rho_{i,new}^{(n)} = \rho_i^{(n-1)} + \varepsilon(\rho_i^{(n)} - \rho_i^{(n-1)}) \quad (11)$$

where $0 < \varepsilon < 1$ is a band-dependent relaxation parameter, and values $\rho_i^{(n)}$ are calculated from (10). The algorithm seeks the minimum of RMSE_L . If the RMSE_L of an iteration exceeds the previous value, the algorithm returns to the previous step and repeats the iteration with a smaller relaxation parameter ε . This semi-empirical strategy ensures quick convergence, usually in 4–6 iterations.

This description shows that the AC algorithm using the MRPV model is much more computationally intensive than the one based on the LSRT model. In each iteration, it requires the azimuthal expansion of the BRF and the calculation of integrals in (2)–(5) for each pixel. In summary, for both LSRT and MRPV models our algorithm finds 1) the best-fit parameters of BRF model, 2) the BRF in MISR view angles, and 3) surface albedo, for every surface pixel of the study area.

C. Ancillary Data and Numerical Aspects

1) *AERONET Data*: AERONET sunphotometers sample the direct solar radiation each 15 min, and sample diffuse sky radiance over a wide range of angles every 60 min during the daytime. AERONET's automated processing system generates AOT and column water vapor from the direct solar measurements, except when the sun is obscured by clouds [4], [22]. Typical AOT uncertainty for a field instrument is 0.01–0.02 and is spectrally dependent. The inversion algorithm [12] uses almucantar sky measurements to retrieve aerosol microphysical properties (particle size distribution and complex refractive index) and concentration. After cloud screening [22], AERONET applies several tests to ensure more reliable retrievals, such as $\text{SZA} \geq 45^\circ$, $\text{AOT}_{0.44} \geq 0.4$, and that there were at least 21 independent angles used in each inversion. These tests analyze sensitivity of retrievals to the single scattering albedo, and to the phase function at large scattering angles. The validity of the Mie aerosol scattering theory in each case is verified by the ‘‘sphericity’’ test, which ensures the cumulative difference between the sunphotometer's sky measurements and the calculations is sufficiently low (i.e., $\text{RMSE}_{\text{sky}} \leq 5\%$) [13]. These quality assurance tests significantly reduce the number of inversion records, as compared to the number of AOT records.

Our algorithm starts with the selection of AERONET aerosol optical thickness and column water vapor values within 15–30 min of the EOS TERRA overpass time. If the conditions described above are met during a day of MISR measurements, the algorithm selects inversion record with aerosol microphysical parameters and size distribution. Otherwise, it uses an aerosol climatology model for a given location derived from multiyear AERONET statistics of reliable retrievals [14]. For example, the climatology model is always used in our algorithm for clear atmospheric conditions (currently defined as $\text{AOT}_{0.44} \leq 0.3$), when it represents the background aerosol.



Fig. 1. Fine resolution Landsat image of the test sites (left) Mongu and (right) GSFC, acquired on April 10, 2000, and August 2, 2001, respectively. The circles show approximately the locations of the “urban” and “green” pixels selected for detailed study. The square on the right image shows the location of the AERONET sunphotometer.

The aerosol climatology model is available for both the GSFC and Mongu locations. For Mongu, we modified the model (“African Savannah, Zambia”) to reduce aerosol absorption in clear conditions, because this model is physically tuned to the smoke from biomass burning which has higher absorption. The described use of aerosol climatology in our processing algorithm significantly improved the stability of the time series of surface albedo (see Section III).

2) *Numerical Aspects of Processing*: Following the selection of aerosol parameters, the algorithm calculates the aerosol optical thickness, single scattering albedo, and scattering phase function with MIE code of W. Wiscombe [15]. The integration over the aerosol size distribution is performed with a 2001-point Simpson’s quadrature. The Mie calculations prescribe the spectral dependence of extinction in the wavelengths of interest, though the magnitude of AOT_{MIE} may differ from the AOT obtained from the AERONET direct solar measurements within 15 min of the satellite overpass. For this reason, AOT_{MIE} is further scaled by fitting to the measured AOT at three wavelengths of the AERONET CIMEL sunphotometer (0.44, 0.67, and $0.87 \mu\text{m}$). MIE calculations are performed for five grid wavelengths across each MISR spectral band in order to compute the band-average radiation functions of (1)–(5), such as path radiance, direct transmittance for a specific incidence-view geometry and others. For example, the band-average path radiance is calculated as

$$D^{\Delta\lambda} = \frac{\int_{\Delta\lambda} S_{\lambda} D_{\lambda} h_{\lambda} d\lambda}{\int_{\Delta\lambda} S_{\lambda} h_{\lambda} d\lambda} \quad (12)$$

where h_{λ} is the spectral band-pass function of a given MISR channel, and the monochromatic path radiance is calculated with the SHARM [16] code for unitary solar illumination

($S_{\lambda} = 1$). Spectral integration in (12) is performed with the step of the solar irradiance database (1 cm^{-1}). The band-pass function and path radiance are evaluated in the integration points by linear and cubic spline interpolation, respectively. This approach allows us to accurately account for spectral variation of the aerosol optical properties and the weak variation of gaseous and water vapor absorption across MISR channels. The zenith-angle integration in (2)–(5) uses 19-point Gaussian quadrature. The azimuthal integration is most efficiently performed by summing an azimuthal Fourier expansion series. The relative accuracy of our calculations is several tenths of a percent.

We processed an area of 32×32 of 1.1-km pixels around each AERONET site. The cloud free conditions with horizontally homogeneous atmosphere are selected with help of the MISR cloud mask and a visual inspection of images.

III. ASSESSMENT OF MISR BRF AND ALBEDO

A. Study Area

Mongu, Zambia ($-15^{\circ}15'S$, $23^{\circ}09'E$), is located on the eastern edge of the Zambezi River floodplain, at the altitude of 1.1 km. Due in part to its exposed sandy soil, Mongu can be seen in a Landsat image (Fig. 1, left) as the brighter area extending into the darker, north-south trending floodplain. The vegetation in the floodplain is mostly grasses or subsistence crops with intermittent seasonal marshes. The higher ground around Mongu is subsistence and commercial cropland to the north and primarily Kalahari woodland to the south. The seasonal reflectance dynamics of the area are seen clearly in Fig. 2, which shows a time series of surface albedo derived from MISR measurements with our algorithm. The upper row shows the true color images composed with equal weights

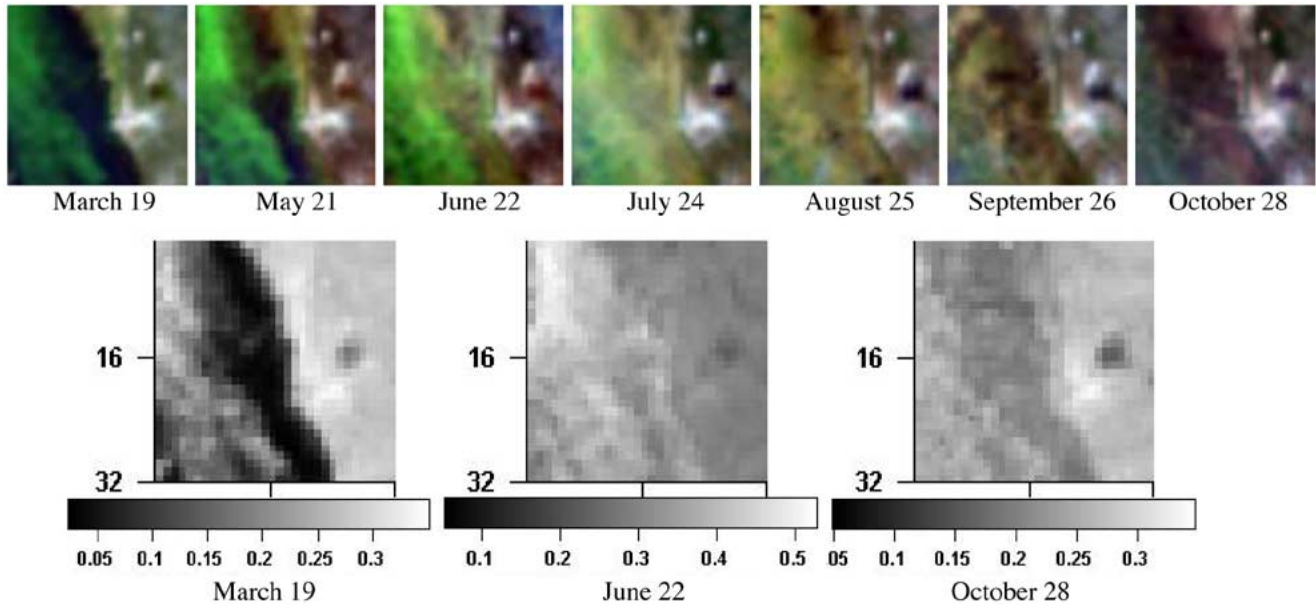


Fig. 2. Temporal dynamics of surface albedo over the test site Mongu in 2003. The albedo was derived from MISR measurements using AERONET ancillary information for the area of 32×32 pixels at resolution of 1.1 km. The upper row shows the true color images composed from equally weighted red, green, and blue bands, and the bottom row shows albedo in the NIR MISR channel.

from the red, green, and blue bands, and the bottom row shows spectral albedo in the near-IR MISR band. The Zambezi River inundates the floodplain, seen as the elongated dark area in both the visible and near-IR images, through May. It dries out in June, which gives way to the fast growth of grasses. In June–July, the area is green in the visible spectrum, with high near-IR albedo and high normalized difference vegetation index (NDVI; an indicator of vegetation health and abundance). By September–October, the grasses die and loose greenness, which is accompanied by a significant reduction of the near-IR reflectance. These changes are easy to observe in the time series of Fig. 2 relative to Mongu’s urban landcovers (primarily buildings, roads and bare soil) whose reflectance exhibits little seasonal change in either the visible or the near-IR spectral regions (see Fig. 6).

The atmosphere is relatively clear in the first half of the dry season (March through mid-June). Local agricultural practices result in extensive biomass burning, especially on the floodplain and nearby grassland dambos, in the late dry season (August–September). The fires lead to high AOT levels. The moderately high AOT values periodically observed in June–July are probably caused by small cooking fires [17]. The wet season, beginning in November, has frequent cloud cover.

Goddard Space Flight Center ($39^{\circ}01'N$, $76^{\circ}52'W$) is located in Greenbelt, MD, a northeast suburb of Washington, DC (Fig. 1, right). The area is a mixture of urban residential area, small deciduous leaf forests, and agricultural cropland. Typical aerosol concentrations and column water vapor are minimal in winter. They increase in summer, reaching maximum in July–August [17].

In this study, we processed 23 days of MISR data over Mongu and 12 days of data over GSFC from 2003 through September 2004. The Langley Data Center provides subsetted data from the direct pass only, once in 16 days. For this reason, the data we

collected essentially comprise all cloud-free subsets of MISR Collection 4 data available at the time of this work.

B. Analysis of MISR BRF

We provide several examples of retrievals to show the algorithm’s performance under different conditions, and to compare our results with the MISR BRF product. For this specific analysis, we selected two pixels for Mongu that display very different temporal behavior—a relatively bright and stable “urban” pixel near the center of town [pixel (19,21)], where the AERONET sunphotometer is also located, and a “green” pixel in the neighboring flood area [pixel (27,9)]. Locations of these pixels are shown by circles in Fig. 1. Similarly, two pixels were selected for the GSFC site displaying lowest and highest NDVI as derived from the retrieved spectral albedos. In the following, we will be comparing the BRF retrieved by our MRPV algorithm at MISR view angles (BRF_{Aer}) with the MISR BRF product (BRF_{MISR}). Because we are using the MISR direct pass data only where the orbit repeats, our analysis is free from the errors of spatial/temporal misregistration.

The results at Mongu for two clear days of March 18, 2003 ($SZA = 30^{\circ}$, $AOT_{0.44} \cong 0.085$) and July 8, 2003 ($SZA = 45.7^{\circ}$, $AOT_{0.44} \cong 0.078$) are shown in Fig. 3. The top plots show MISR normalized radiance (L/S_{λ}) against our calculations with the best-fit MRPV model. The residual mean-square difference for the radiance is low ($1.2 < RMSE_L < 2.4\%$) except for the “green” pixel in the near-IR, where $RMSE_L \cong 7\%$ and BRF model does not fit the surface reflectance particularly well. The MISR BRF, retrieved BRF_{Aer} , and the best-fit MRPV values are shown in the middle and bottom plots. The goodness-of-fit is evaluated with the value $RMSE_{\rho}$. With the exception of the blue band, the $RMSE_{\rho} \leq 10\% - 15\%$ usually implies that the BRF model fits observations well. Fig. 3 shows that our results generally agree with the MISR BRF, although there are

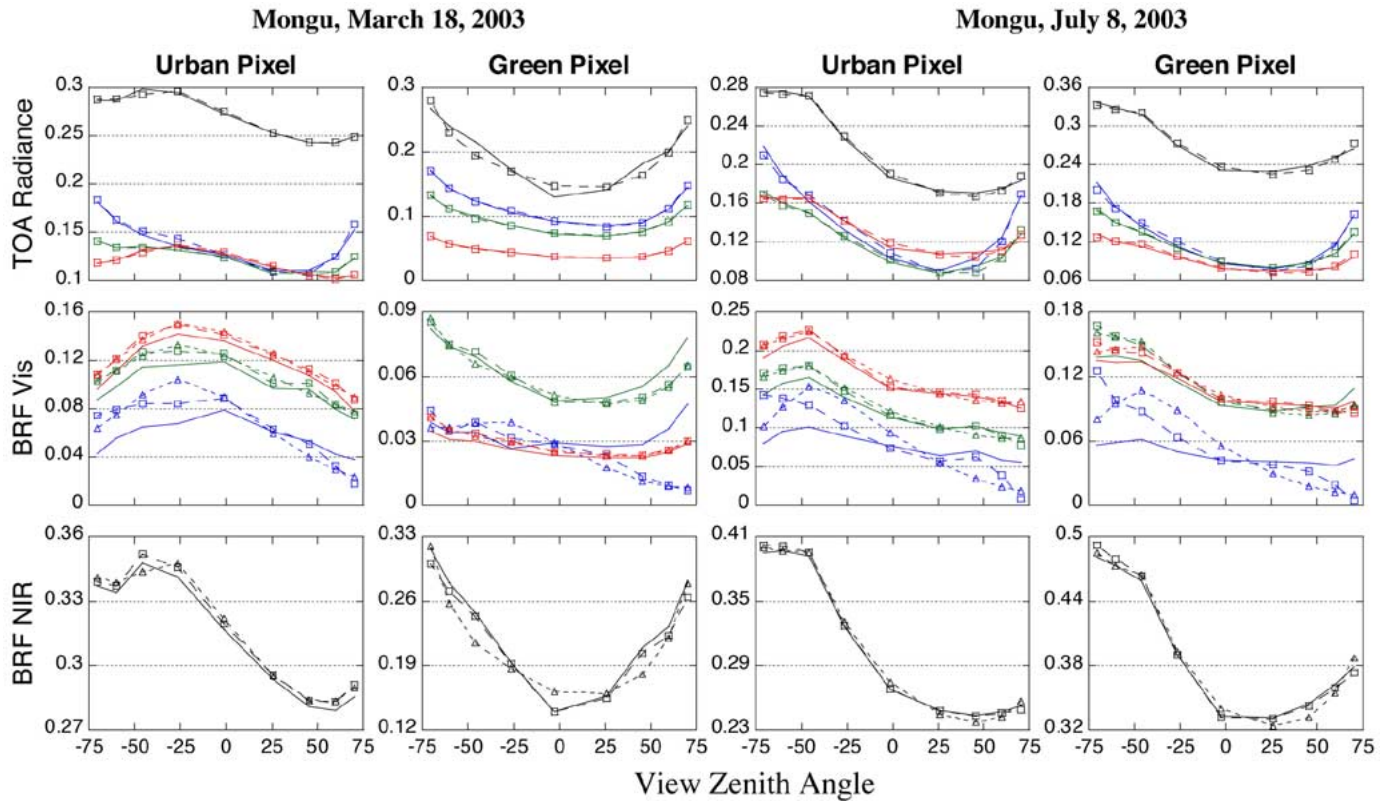


Fig. 3. TOA radiance and BRF for “urban” and “green” pixels, Mongu, on March 18, 2003 and July 8, 2003. (a) The top plots show (solid lines) normalized MISR radiance and (squares connected by dashed lines) computed TOA radiance with the best-fit MRPV model. The blue, green, and red bands are shown by their respective colors, and NIR band is shown in black. (b) The middle plots show (solid lines) MISR BRF, (squares) the retrieved BRF, and (triangles) the calculated MRPV model with the best-fit parameters, in the blue, green, and red bands. (c) The bottom plots are the same as the middle plots, only for the NIR band. The positive/negative values on X axis represent forward/back-scattering directions (aft/fore MISR cameras).

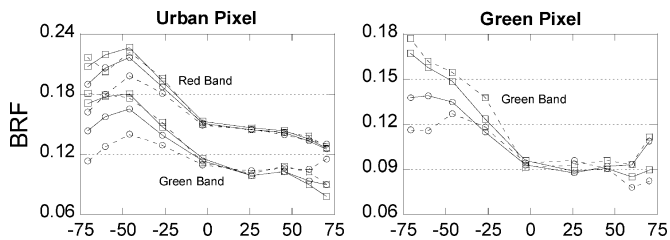


Fig. 4. Comparison of BRF retrieved on (solid lines) the clear day of July 8, 2003 and (dashed lines) the hazy day of July 24, 2003 over Mongu. Squares show BRF_{Aer} retrieved with the MRPV algorithm, and circles represent BRF_{MISR} .

some systematic differences in that the latter is less asymmetric between the forward and back-scattering directions.

Another example of comparison of retrievals for July 8, 2003 and July 24, 2003 is shown in Fig. 4. On these days separated by a 16-day interval, the sun angle changes little (45.7° and 43.9°), but the atmospheric conditions change from clear ($AOT_{0.44} \cong 0.078$) to hazy ($AOT_{0.44} \cong 0.53$). Our retrievals and the MISR BRF for July 8 (solid line) and July 24 (dashed line) are shown by squares and circles, respectively. In the left panel, the results are plotted for the “urban” pixel in the green and red bands, and the right panel shows comparison for the “green” pixel in the green band only (results for the red band are similar). One can see the consistency of BRF_{Aer} both in shape and degree of asymmetry on these two days, especially for the “urban” pixel where surface conditions change little during the

middle of the dry season. The BRF_{MISR} is consistent for the narrower range of angles, with a larger discrepancy in the backscattering directions.

Our results for the GSFC site are similar to those found for Mongu.

C. Origins of BRF Discrepancy

The examples of Fig. 3, and our results for other days, show that there is a systematic discrepancy, namely BRF_{Aer} is more asymmetric than BRF_{MISR} in the visible bands. The difference decreases with wavelength and becomes negligible in the near-IR. The found discrepancy roots in the MISR operational algorithm and most likely is caused by the following two reasons. First, in the MISR hemispherical-directional reflectance factor (HDRF) algorithm, which precedes BRF retrieval, the iteration loop is currently turned off. This loop removes the influence of the upward diffuse transmittance on the retrieved HDRF. Turning off this loop suppresses the full angular dependence, and reduces anisotropy of both HDRF and BRF. The effect grows with the atmospheric optical depth; therefore, both reflectance functions are more flattened in the blue band than in the near-IR band. The iteration is currently turned off because at large AOT the surface reflectance signal is small and the HDRF retrieved with a full iteration often takes negative values in the extreme view angles ($\approx 70^\circ$), where the role of uncertainties is the largest. Currently, the modified form

of the iteration process is being tested for future versions of the MISR surface retrieval algorithm.

Second, the refined MISR aerosol algorithm over land uses the assumption of spectral invariance of surface directional reflectance. This algorithm seeks aerosol models for which the angular shapes of HDRF are most similar in the four MISR spectral bands [18]. In the merit function, the departure from the common shape is most heavily penalized in the blue band, and least in the near-IR. Thus, the best-fit aerosol model, for example, will bias the HDRF shape in the blue band toward that of in the red and near-IR bands, though it does not require angular shapes to be exactly the same across all bands. This postlaunch refinement allowed MISR to achieve better correlation of AOT with AERONET measurements globally, reduce the number of outliers, and improve the selectivity of the aerosol model from the large number of candidates [18]. In our analysis over Mongu and GSFC, we found that with rare exception the MISR AOT and Angstrom parameter were very close to those retrieved from AERONET data, in agreement with the analysis of Kahn *et al.* [19] on global MISR aerosol product validation.

Most of the examples given above indeed show the commonality of MISR normalized BRF shapes in the blue, green and red bands caused by the assumption of spectral invariance. This assumption relies on the fact that surface scattering elements (e.g., soil grains, leaves) are much larger than the wavelength. Theoretically, this assumption is valid for light scattered once, and it becomes less reliable when multiple scattering occurs. Multiple scattering smoothes the angular anisotropy of reflectance, which is largely defined by the relative weight of the single versus multiple scattering. Their ratio strongly depends on the absorption of the surface. Therefore, the assumption of spectral invariance would be valid if surface absorption did not depend on wavelength. Commonly, most land surfaces absorb strongly in the blue wavelengths, and even more strongly in the ultraviolet part of spectrum—a consequence of chlorophyll absorption in vegetation and iron molecule absorption in soils. This reduces the multiple scattering and increases reflectance anisotropy at these shorter wavelengths. Our retrievals indeed suggest that surfaces are usually most anisotropic in the blue wavelengths, and least anisotropic in the near-IR. On the other hand, the difference is not large. Overall, the MISR BRF is close to BRF_{Aer} , in particular in the green, red and near-IR wavelengths, which are important in land studies involving vegetation analysis.

The first author also investigated the error of a simplifying assumption of using only two azimuthal harmonics in the Fourier expansion of the BRF in the operational MISR land algorithm [10]. A specific example for July 8, 2003 (Mongu, “urban” pixel) is given in Fig. 5. It shows the equivalent difference in the BRF (ΔBRF) corresponding to the error in TOA radiance of the truncated two-term solution. The truncated solution is higher, and the difference has a V-shape, which is almost symmetric about nadir. Therefore, the MISR BRF should be symmetrically lower than the accurate BRF, increasingly at higher view zenith angles, in order to compensate for this difference. This also reduces MISR albedo, creating a systematic bias. The magnitude of ΔBRF is very small in clear conditions, but it grows with AOT. The error (ΔBRF)

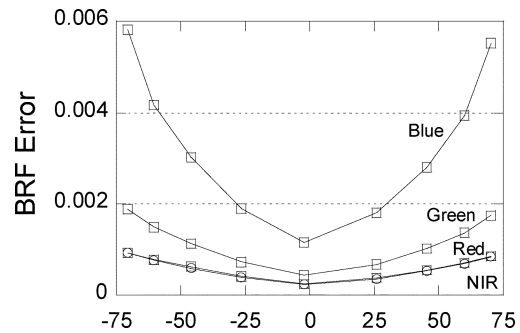


Fig. 5. Equivalent ΔBRF corresponding to the difference between the approximate and accurate TOA radiance calculated in MISR spectral bands for the “urban” pixel on July 8, 2003. The approximate solution is obtained with two azimuthal harmonics in the lower boundary condition. The blue, green, and red bands are shown by squares, and NIR band is shown by circles.

calculated for July 24 was five times larger for all bands than that shown in Fig. 5. This can explain about 20%–30% of the change in BRF_{MISR} from the clear to the hazy day in Fig. 4. Yet in most cases, this error remains small and has little impact on MISR land retrievals.

D. Analysis of Albedo

The surface albedo in our algorithm is defined as a ratio of reflected radiative flux to the incident flux at the surface level. The equivalent MISR product is bi-hemispherical reflectance (BHR).

Throughout this work, we found that examining the time series of surface albedo allows us to better evaluate the quality of our retrievals. The examples of the albedo time series for the “urban” and “green” pixels of Mongu and GSFC sites are given in Fig. 6 (middle and bottom plots). The retrieved albedo (with MRPV algorithm) is shown by squares connected by a dashed line, and the MISR albedo is shown by triangles connected by a solid line. The top plots of Fig. 6 show the solar zenith angle, and give a comparison of AOT measured by AERONET and retrieved by MISR in the blue and red bands. The left plot shows a significant variability and high AOT values over Mongu in the second half of the dry season.

Fig. 6 shows a large difference in the magnitude of temporal variability between the “urban” and “green” pixels, Mongu, in the red and near-IR bands. During the early and middle of the dry season, albedo increases monotonically over time in the visible bands. This likely results from the gradual drying of the sandy soils together with the loss of absorbing pigments in the vegetation as it senesces. Later, as leaf loss occurs, more of the bright sandy soil becomes visible from satellites. The difference between the “urban” and “green” pixels is also clearly seen for the GSFC site. Here, the magnitude of seasonal variability is mitigated, because at the small-scale variability of surface typical for GSFC scene (see Fig. 1) the pixels of study contain both vegetation and urban elements of the residential area (roofs, asphalt, concrete, etc.).

The albedo retrieved by our algorithm in the blue band is relatively noisy; on hazy days it was found to be higher than would be predicted by the preceding time series based on clear days. Analyzing these cases, we found that AERONET retrievals showed high aerosol absorption (single scattering

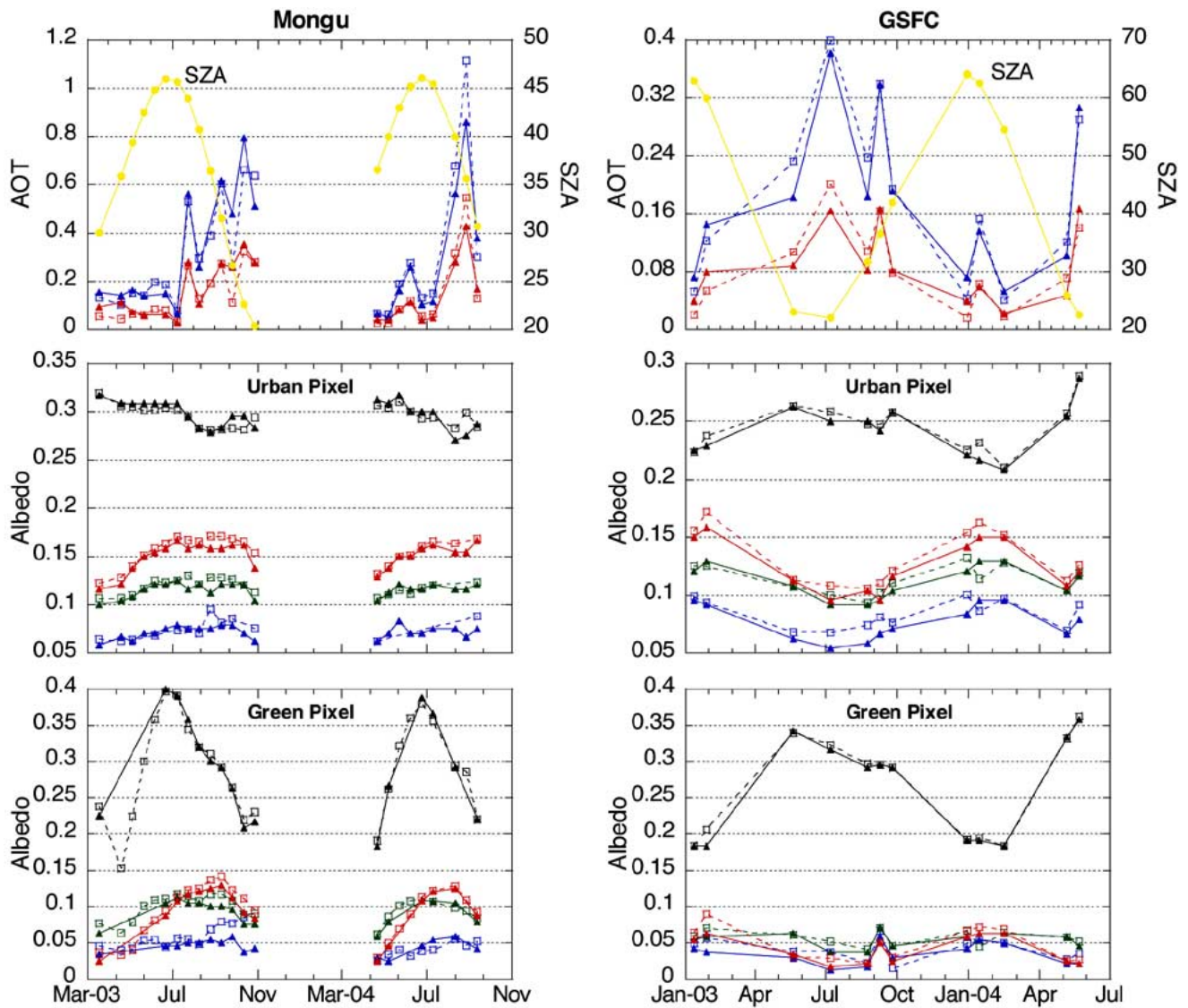


Fig. 6. Time series of surface albedo for the “urban” and “green” pixels (left) over Mongu and (right) over GSFC. The top plots show (\blacktriangle) MISR AOT in the blue and red bands as compared to (\square) AERONET AOT and a solar zenith angle. The middle and bottom plots show surface albedo retrieved with (squares connected by dashed lines) the MRPV algorithm and (triangles connected by solid line) the MISR albedo product.

albedo at $0.44 \mu\text{m}$ lower than ≈ 0.86) in each case. At the same optical thickness, higher absorption reduces path radiance, and our algorithm has to artificially boost surface reflectance to compensate for the difference. The sensitivity to the aerosol absorption and jitter in the retrieved albedo increase with aerosol optical thickness. To reduce the noise, we repeated AERONET inversions over Mongu for all hazy days, and selected the least absorbing inversions that satisfied the quality assurance constraints described in Section II-C1. Reprocessing was conducted with the new Version 2 software that improves inversions, and also with our previously retrieved average surface albedo for Mongu which substituted the default values of AERONET database. This effort led to lower aerosol absorption in the AERONET data, and improved our retrievals for five of seven hazy days, at least in the green and red bands. However, for two hazy days in 2004, the derived albedo remained unacceptably high.

Except for clear atmospheric conditions, our retrievals in the blue band are very sensitive to the magnitude of the AERONET

aerosol absorption. For this reason, we presently do not consider these data highly reliable and do not provide further analysis. On the other hand, this high sensitivity could potentially be used in the joint inversion of AERONET and space-borne measurements as a physical constraint on the blue band absorption. This constraint is envisioned in the form of *a priori* thresholds on the retrieved surface albedo that can be predicted from the previous time series over relatively stable pixels.

Fig. 6 shows that MISR albedo in the visible bands is slightly lower than the albedo we retrieved over both Mongu and GSFC sites. In the green and red bands, the average bias is $\Delta q \cong 0.005$. In most cases, the bias can be partly explained by the lower absorption of the aerosol model selected in the MISR algorithm as compared to the AERONET-derived aerosol absorption. On average, the MISR single scattering albedo was 0.91 compared to 0.88 from AERONET over Mongu, and 0.995 compared to 0.97 over GSFC. The operational assumptions of MISR algorithm discussed earlier may also contribute to this bias. The offset in the red band, though relatively small, may af-

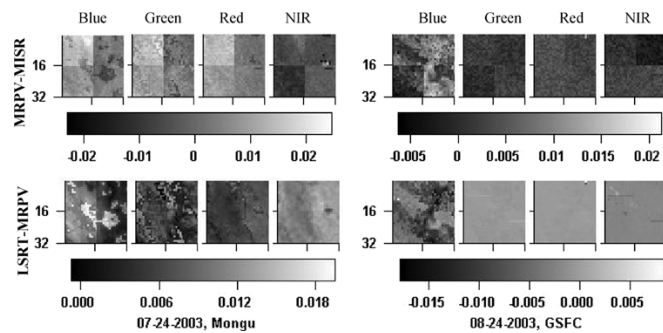


Fig. 7. Spatial distribution of albedo difference (left) for Mongu on July 24, 2003 and (right) for GSFC on August 24, 2003. The top row of images shows the difference between albedo retrieved with the MRPV model and the MISR product. The bottom row shows the albedo difference between the LSRT and MRPV models.

fect vegetation indices and higher level land products (e.g., leaf area index) [20].

The MISR albedo fully reproduces the temporal trend. The jitter we observed in our retrievals in the blue band is small; analysis shows that MISR aerosol algorithm consistently selected aerosol models with the single scattering albedo well constrained between 0.87 and 0.95 at $0.44 \mu\text{m}$ over Mongu. Remarkably, MISR provides rather accurate surface retrievals under heavy aerosol conditions in all bands (Fig. 6), e.g., for August 11, 2004 and August 27, 2004, where our MRPV algorithm failed in the blue and green bands. This is clearly a consequence of the MISR robust aerosol retrievals.

In the following step, we broadened analysis by including the whole study area of 32×32 pixels in the comparison. This adds spatial heterogeneity to the study area and provides an opportunity to analyze mosaic effect in the MISR surface reflectance. Mosaic has its origins in MISR performing aerosol retrievals at a scale of 16×16 pixels, which creates independent offsets in four quadrants covering the study area. The spatial distributions of albedo difference ($q_{\text{Aer}} - q_{\text{MISR}}$) for Mongu on 7/24/2003 (hazy day) and for GSFC on 8/24/2003 (clear day) are shown in Fig. 7 (top row). The difference is relatively homogeneous within each of the four 16×16 quadrants, with the pixel-to-pixel variation less than 0.004. In hazy conditions, mosaic effect caused by MISR aerosol retrievals creates a larger variability (up to 0.015–0.02) at a coarse scale of 17.6 km.

IV. COMPARISON OF RETRIEVALS WITH LSRT AND MRPV BRF MODELS

A. Effect of BRF Model on Retrieved BRF

Earlier (Section II-B), we compared efficiency of surface retrieval algorithms based on LSRT and MRPV models. The retrieval results are also affected by the choice of the BRF model according to its ability to fit variety of natural BRF shapes, and, for example, its behavior at high zenith angles.

Generally, the BRFs obtained with the MRPV and LSRT models are very similar. For example, Fig. 8 compares the retrieved BRFs and the best-fit values of the two models for the red and near-IR bands on March 18, 2003 and July 8, 2003. One can see that the MRPV model fits retrieved BRF uniformly well on both days, whereas the LSRT model does not

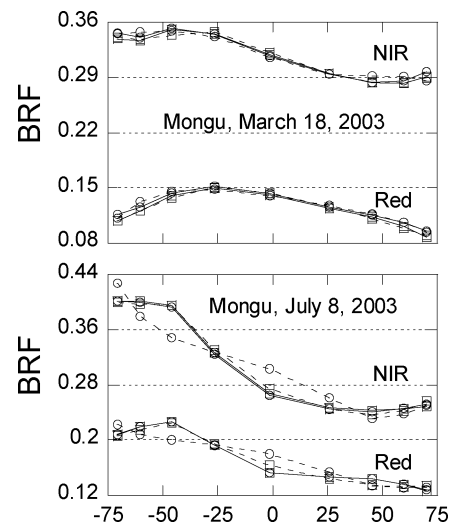


Fig. 8. (Solid line) Retrieved BRF and (dashed line) the calculated best-fit BRF model for the “urban” pixel, Mongu. The squares and circles represent MRPV and LSRT models, respectively.

provide a good fit for July 8, giving the high values of RMSE_ρ . Despite the difference in the fit, the retrieved BRFs remain very close between the two models. This relative insensitivity is explained by two factors. First, in clear atmospheric conditions, the diffuse radiance is relatively small compared to the direct surface-reflected radiance except when the solar zenith angle is high. Second, the diffuse reflected radiance is a smooth function of angle due to the angular redistribution of energy. As such, it is more sensitive to the average magnitude of reflectance rather than to the angular idiosyncrasies of the BRF models as long as both models adequately predict the general shape of the BRF.

In the green, red, and near-IR bands, our results suggest the MRPV model generally provides a slightly better fit. In the blue band, the retrieved BRF is often more anisotropic than in the green or red bands, and the ratio between the maximum and the minimum of BRF values may be several times larger than that at longer wavelengths. The LSRT model fits such shapes reasonably well, whereas the MRPV model often does not provide an adequate fit ($\text{RMSE}_\rho \approx 30\% - 50\%$), which leads to unreasonably low or high albedo.

B. Effect of BRF Model on Retrieved Albedo

Comparing retrievals with the LSRT and MRPV models, we found that they provide similar albedo, within about ± 0.005 in the visible bands, and ± 0.015 in the near-IR band, when the models fit their corresponding BRF well ($\text{RMSE}_\rho \leq 10\% - 15\%$). Our results indicate that the sign of the albedo difference between these models is site dependent. For example, the LSRT albedo was systematically higher than the MRPV albedo in the visible spectrum over Mongu, but was lower over GSFC. The same relationship holds for the retrieved BRF. Most probably, this relationship is mediated by aerosol absorption, which is consistently higher over Mongu. The higher absorption changes the angular distribution of incident diffuse radiance, especially at higher zenith angles. Thus, it may impact the diffuse surface-reflected radiance because the MRPV and LSRT models behave differently at higher angles. In the near-IR band, the

LSRT albedo was higher than MRPV albedo for both sites, by 0.01 over Mongu, and by 0.002 over GSFC. We will further study the agreement of albedo and BRF between the two models with accumulation of statistics for additional sites.

The spatial distribution of the albedo difference between the LSRT and MRPV models is shown in Fig. 7, bottom row. With the exception of the blue band, the difference is rather homogeneous, with variation across the images less than ≈ 0.004 on the hazy day and ≈ 0.002 on the clear day. The absence of notable variability means that the image of surface albedo does not contain model-dependent distortions from the variable land cover.

V. CONCLUSION

In this paper, we reported the first results of independent AC of MISR measurements over small areas around AERONET sunphotometer sites using aerosol parameters and column water vapor from AERONET as well-calibrated ancillary information with established accuracy. With this approach, we are able to indirectly test correctness of MISR aerosol retrievals and accuracy of the AC algorithm. Indirect validation of the MISR BRF and albedo with our data is done at the same spectral and spatial resolution, which addresses an unresolved problem of ground-based validation over heterogeneous surfaces. Our approach, if supported by periodic ground-based measurements over stable homogeneous test sites with different levels of surface brightness that would establish an absolute reference for the BRF and albedo, can be considered a full validation that is easily expandable at the regional and global level given the AERONET global infrastructure.

As an initial demonstration of this concept, we conducted a local analysis of MISR BRF and albedo products over two sites, GSFC (Greenbelt, MD) and Mongu (Zambia), for available MISR direct pass data of Collection 4 for 2003–2004. Making independent retrievals with LSRT and MRPV models of BRF, we also studied the impact of a model on retrieved BRF and albedo. Since the LSRT model is used in the MODIS land algorithm, and the MRPV model is a basis for MISR surface retrievals, such study is an important step to understanding differences between the MISR and MODIS global surface reflectance products that arise in part from the difference in models.

Summary results from this study include the following.

- 1) A comparison of our retrievals with the MISR BRF and albedo showed a close agreement. MISR retrieves correct BRF shapes, fully reproduces the temporal pattern of albedo and BRF, and provides accurate retrievals in difficult cases of high AOT. Among differences we found, the most important are the following.
 - MISR BRF overall is less anisotropic in the visible bands. The difference is greatest in the blue band, decreases in the green and further in red bands, and is negligible in the near-IR band. This discrepancy originates in part in the MISR aerosol retrieval algorithm over heterogeneous land, which tends to select an aerosol model that benefits the spectrally invariant shapes of the surface BRF. The other part of discrepancy comes from

the surface HDRF retrieval algorithm where the iteration loop that removes the diffuse atmospheric transmittance is currently turned off. An additional small contribution may be added from the approximate calculation of diffuse surface-reflected radiance with only two azimuthal harmonics in the MISR algorithm at high AOT; otherwise, this error is negligible.

- MISR albedo was on average smaller by about 0.005 in the green, red and near-IR bands. When significant aerosol absorption is present (Mongu), the albedo discrepancy is additionally biased by the difference between the MISR-retrieved and AERONET estimates of aerosol absorption (single scattering albedo).
 - MISR albedo accurately reproduces the areas' spatial distribution of albedo. The pixel-to-pixel difference with our retrievals does not exceed ≈ 0.004 in all bands. A larger spatial variation (~ 0.015 – 0.2) in the form of mosaic may develop at a coarser resolution (17.6 km), mainly in hazy conditions, as a consequence of MISR aerosol retrievals at this scale.
- 2) Comparison of our retrievals performed with the MRPV and LSRT models showed the following.
 - Overall, the models have approximately the same capacity to fit the BRF shapes derived for GSFC and Mongu sites at MISR view geometries, though MRPV model is generally preferable except in the blue band. On the other hand, due to its linearity, the LSRT model offers a significant advantage in the processing speed.
 - The albedos from the two models are generally similar, within 0–0.015, with the average difference ≤ 0.005 . We found that the relationship between them is site-dependent, or, in other words, it is most probably a function of aerosol absorption. The albedo from the LSRT model was systematically higher in medium and high aerosol absorption cases (Mongu), whereas MRPV albedo was higher in low aerosol absorption cases (GSFC).

Overall, our analysis leads us to conclude that MISR Collection 4 offers high quality surface reflectance products. Of the mentioned errors, the found small negative albedo bias of 0.005 is probably the most important one, if confirmed by our further research. The larger error in a form of mosaic caused by aerosol retrievals has presumably a random nature, and can be removed in a time series analysis by simple smoothing procedures, or in the time-composite global products. One should keep in mind that presented initial evaluation of MISR surface reflectance is based on a very limited number of processed cases, and serves more to demonstrate our approach rather than to give conclusive accuracy statements. In the near future, we plan to significantly increase the number of AERONET sites in our processing, which will broaden the range of land cover types and atmospheric conditions, and to extend our approach to a regional and then global scale.

There is still a significant amount of work to be done with our algorithm. For example, the BRF of the LSRT model often takes negative values at high angles, which are used in integration. A “transient” model that fixes this problem was proposed in [21], and we plan to explore its use in our algorithm. We will

continue algorithm development to improve the reliability and accuracy of our retrievals in the MISR blue band, and in high AOT cases. Our present algorithm works with spherical aerosol particles only, although AERONET provides retrievals for both spheres and spheroids. The assumption of sphericity works well for both the GSFC and Mongu locations and does not affect the results presented here. However, adding the nonspherical solution to our algorithm will extend the algorithm performance to the world locations where dust transport plays an important role. In the near future, we will start running the full 3-D version of the processing algorithm that takes an adjacency effect into account. We also look forward to the expected improvements in AERONET processing, such as introducing the next Version 2 software as operational, and updating the surface reflectance database which should improve quality of inversions.

ACKNOWLEDGMENT

A. Lyapustin would like to thank D. Diner and R. Kahn, JPL, for very useful discussions and suggestions.

REFERENCES

- [1] M. King and R. Greenstone, Eds., *EOS Reference Handbook: A Guide to Earth Science Enterprise and the Earth Observing System*. Greenbelt, MD: EOS Project Science Office, NASA/Goddard Space Flight Center, 1999, p. 355.
- [2] J. T. Morisette, J. L. Privette, and C. O. Justice, "A framework for the validation of MODIS land products," *Remote Sens. Environ.*, vol. 83, pp. 77–96, 2002.
- [3] J. V. Martonchik, "Retrieval of surface directional reflectance properties using ground level multiangle measurements," *Remote Sens. Environ.*, vol. 50, pp. 303–316, 1994.
- [4] B. N. Holben, T. F. Eck, I. Slutsker, D. Tanré, J. P. Buis, A. Setzer, E. Vermote, J. A. Reagan, Y. J. Kaufman, T. Nakajima, F. Lavenue, I. Jankowiak, and A. Smirnov, "AERONET-A federated instrument network and data archive for aerosol characterization," *Remote Sens. Environ.*, vol. 66, pp. 1–16, 1998.
- [5] A. Lyapustin and Y. Knyazikhin, "Green's function method in the radiative transfer problem. I: Homogeneous non-Lambertian surface," *Appl. Opt.*, vol. 40, pp. 3495–3501, 2001.
- [6] —, "Green's function method in the radiative transfer problem. II: Spatially heterogeneous anisotropic surface," *Appl. Opt.*, vol. 41, pp. 5600–5606, 2002.
- [7] W. Lucht, C. B. Schaaf, and A. H. Strahler, "An algorithm for the retrieval of albedo from space using semiempirical BRDF models," *IEEE Trans. Geosci. Remote Sens.*, vol. 38, no. 2, pp. 977–998, Mar. 2000.
- [8] C. B. Schaaf *et al.*, "First operational BRDF, albedo nadir reflectance products from MODIS," *Remote Sens. Environ.*, vol. 83, pp. 135–148, 2002.
- [9] J. V. Martonchik, D. J. Diner, B. Pinty, M. M. Verstratete, R. B. Myneni, Y. Knyazikhin, and H. R. Gordon, "Determination of land and ocean reflective, radiative and biophysical properties using multiangle imaging," *IEEE Trans. Geosci. Remote Sens.*, vol. 36, no. 4, pp. 1266–1281, Jul. 1998.
- [10] D. J. Diner, J. V. Martonchik, C. Borel, S. A. W. Gerstl, H. R. Gordon, Y. Knyazikhin, R. Myneni, B. Pinty, and M. M. Verstraete, "MISR level 2 surface retrieval algorithm theoretical basis," NASA EOS-MISR Doc., JPL D-11401, Rev. D, NASA JPL, 1999.
- [11] J.-L. Roujean, M. Leroy, and P. Y. Deschamps, "A bidirectional reflectance model of the Earth's surface for the correction of the remote sensing data," *J. Geophys. Res.*, vol. 97, pp. 20 455–20 468, 1992.
- [12] O. Dubovik and M. D. King, "A flexible inversion algorithm for retrieval of aerosol optical properties from sun and sky radiance measurements," *J. Geophys. Res.*, vol. 105, pp. 20 673–20 696, 2000.
- [13] O. Dubovik, A. Smirnov, B. N. Holben, M. D. King, Y. J. Kaufman, T. F. Eck, and I. Slutsker, "Accuracy assessments of aerosol optical properties retrieved from AERONET sun and sky-radiance measurements," *J. Geophys. Res.*, vol. 105, pp. 9791–9806, 2000.
- [14] O. Dubovik, B. Holben, T. F. Eck, A. Smirnov, Y. J. Kaufman, M. D. King, D. Tanre, and I. Slutsker, "Variability of absorption and optical properties of key aerosol types observed in worldwide locations," *J. Atmos. Sci.*, vol. 59, pp. 590–608, 2002.
- [15] W. Wiscombe, "Improved Mie scattering algorithms," *Appl. Opt.*, vol. 19, pp. 1505–1509, 1980.
- [16] A. I. Lyapustin and T. Z. Muldashev, "Method of spherical harmonics in the radiative transfer problem with non-Lambertian surface," *J. Quant. Spectrosc. Radiat. Transf.*, vol. 61, pp. 545–555, 1999.
- [17] B. Holben *et al.*, "An emerging ground-based aerosol climatology: Aerosol optical depth from AERONET," *J. Geophys. Res.*, vol. 106, pp. 9807–9826, 2001.
- [18] D. J. Diner, J. V. Martonchik, R. A. Kahn, B. Pinty, N. Gobron, D. L. Nelson, and B. N. Holben, "Using angular and spectral shape similarity constraints to improve MISR aerosol and surface retrievals over land," *Remote Sens. Environ.*, 2004, submitted for publication.
- [19] R. A. Kahn, B. J. Gaitley, J. V. Martonchik, D. J. Diner, K. A. Crean, and B. Holben, "MISR global aerosol optical depth validation based on two years of coincident AERONET observations," *J. Geophys. Res.*, to be published.
- [20] Y. Knyazikhin, J. V. Martonchik, D. J. Diner, R. B. Myneni, M. M. Verstraete, B. Pinty, and N. Gobron, "Estimation of vegetation canopy leaf area index and fraction of absorbed photosynthetically active radiation from atmosphere corrected MISR data," *J. Geophys. Res.*, vol. 103, no. D24, pp. 32 239–32 256, 1998.
- [21] F. Gao, X. Li, A. Strahler, and C. Schaaf, "Evaluation of the Li Transit kernel for BRDF modeling," *Remote Sens. Rev.*, vol. 19, pp. 205–224, 2000.
- [22] A. Smirnov, B. N. Holben, T. F. Eck, O. Dubovik, and I. Slutsker, "Cloud screening and quality control algorithms for the AERONET data base," *Remote Sens. Env.*, vol. 73, pp. 337–349, 2000.



Alexei Lyapustin received the B.S. and M.S. degrees in physics from Moscow State University, Moscow, Russia, in 1987, and the Ph.D. degree in aerospace remote sensing from the Space Research Institute, Moscow, in 1991.

He is currently an Associate Research Scientist at the Goddard Earth Sciences and Technology Center, University of Maryland, Baltimore County. He actively works on 1-D and 3-D radiative transfer theory. His main research interests are focused on new algorithms for aerosol retrieval and AC of MODIS, MISR, and Landsat data. In 2004, he was selected a Science Team Member for the MODIS and NPP Science Teams.



Yujie Wang received the B.S. and an M.S. degrees in physics from Tsinghua University, Beijing, China, in 1994 and 1998, respectively, and the Ph.D. degree in geography from Boston University, Boston, MA, in 2002.

In July 2002, he joined the Goddard Earth Sciences and Technology Center, University of Maryland, Baltimore County, as a Research Associate. During his Ph.D. studies, his research was focused on the prototyping and validation of radiative transfer-based EOS MODIS LAI/FPAR algorithms. At present, he is developing a surface reflectance validation dataset centered on AERONET sites from the measurements of EOS MISR, MODIS, and future NPOESS VIIRS instrument.



John Martonchik received the Ph.D. degree in astronomy from the University of Texas, Austin, in 1974.

He joined the Jet Propulsion Laboratory, Pasadena, CA, in 1972, where he is currently a Research Scientist with the Multiangle Imaging element of the Earth and Space Sciences Division. His experience includes analyzing telescopic and spacecraft observations of planetary atmospheres, laboratory and theoretical studies of the optical properties of gaseous, liquid, and solid materials, and the development and implementation of 1-D and 3-D radiative transfer and line-by-line spectroscopy algorithms for studies of planetary atmospheres and Earth tropospheric remote sensing. He has been involved in several NASA Land Processes programs, including Remote Sensing Science, FIFE, and BOREAS, and he is presently the Aerosol/Surface product algorithm scientist for the EOS MISR experiment.



Jeffrey L. Privette (M'95) received the B.A. degree from The College of Wooster, Wooster, OH, the B.S. degree from the University of Michigan, Ann Arbor, and the M.S. and Ph.D. degrees in aerospace engineering sciences from the University of Colorado, Boulder.

After postdoctoral work with the University of Maryland, he joined the Biospheric Sciences Branch (Code 614.4), NASA Goddard Space Flight Center, Greenbelt, MD, in 1996. His research has focused on the retrieval of land biophysical parameters via solar-reflective and thermal infrared remote sensing, and he has been active in SAFARI 2000, the MODIS Land Validation Program, the CEOS Working Group for Calibration and Validation, and the NPP/NPOESS project. He is currently Deputy Project Scientist and a science team member for the NPOESS Preparatory Project.



Brent Holben received the M.S. degree from Colorado State University, Fort Collins, in 1976, specializing in biometeorology and remote sensing.

He is currently a Research Scientist at the NASA Goddard Space Flight Center (GSFC), Greenbelt, MD. He was a Staff Scientist with the University of Puerto Rico/Puerto Rico Nuclear Center investigating mesoscale radiation balance in the Luquillo Experimental Forest until 1978 when he joined the NASA GSFC. He has published on remote sensing of vegetation dynamics, ACs to remotely sensed data, and more recently, aerosol optical properties. He is the Project Leader of the ground-based aerosol characterization program AERONET, initiating and guiding its development since 1992.



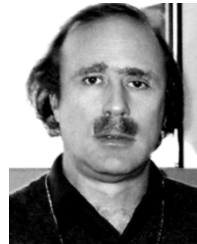
Ilya Slutsker received the B.S. and M.S. degrees in physics and engineering and the Ph.D. degree in physics and mathematics from St. Petersburg Polytechnical Institute, St. Petersburg, Russia, in 1987 and 1991, respectively.

From 1991 to 1992, he was a Programmer with the Leningrad Institute of Precision Mechanics and Optics, St. Petersburg. Since 1992, he has been with the Goddard Space Flight Center, Greenbelt, MD, as a Contractor Programmer/Analyst supporting AERONET.



Alexander Sinyuk received the B.S. and M.S. degrees in physics and theoretical physics from Belarus State University in 1985, and the Ph.D. in Physics/Optics from the Institute of Physics, Minsk, Belarus, in 1997.

In 1998, he became a Research Associate with the Laboratory of Optics of Disperse Medium, Institute of Physics. He was Visiting Scientist with the Laboratory of Meteorological Physics, Universite Blaise Pascal, France, in 1998, and a Visiting Scientist at the Meteorological Research Institute, Tsukuba, Japan, in 1999. Since January 2000, he has been with the Goddard Space Flight Center, Greenbelt, MD, as a Contractor. His research interests include satellite- and ground-based remote sensing, with emphasis on the development of inversion methods of aerosol and surface properties retrieval.



Alexander Smirnov received the degree in physics from St. Petersburg State University, St. Petersburg, Russia, in 1980, and the Ph.D. degree in physics and mathematics from the Institute of Oceanology, Russian Academy of Sciences, Moscow, in 1988, where his major research interest was atmospheric aerosol optical properties over the oceans.

From 1980 to 1991, he was a Scientist, then a Senior Scientist, with the St. Petersburg Hydrometeorological Institute. From 1993 to 1996, he was a Postdoctoral Fellow and Project Scientist at the Universit de Sherbrooke, Sherbrooke, QC, Canada. In June 1996, he joined Science Systems and Applications, Inc., and started working on the AERONET Project. Currently, he is a Senior Research Scientist with the Goddard Earth Sciences and Technology Center, University of Maryland, Baltimore County. His current research interests include ship-borne and ground-based studies of atmospheric aerosols, remote sensing instrumentation, and data analysis.